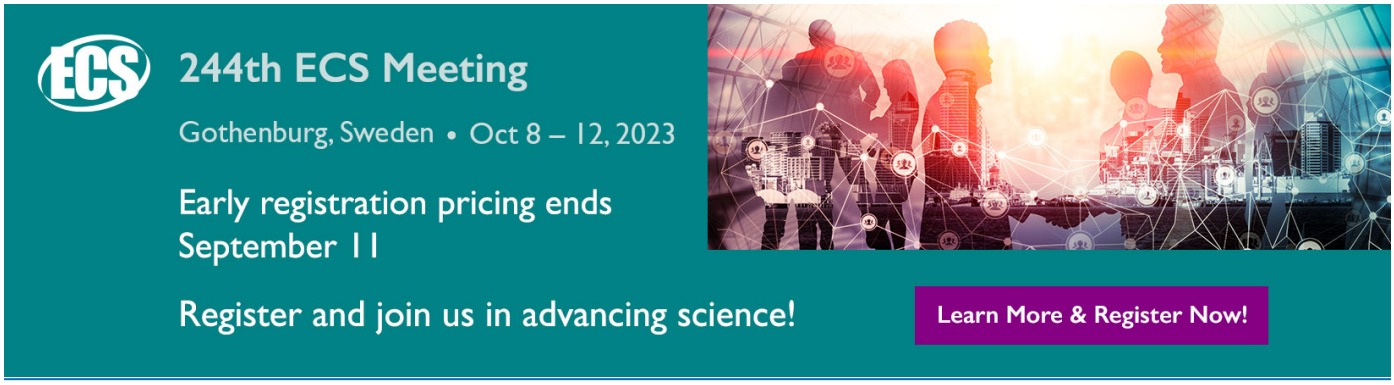
Journal of Physics D: Applied Physics

PAPER • **OPEN ACCESS**

Computer vision assisted decomposition analysis of atom probe tomography data

To cite this article: Janis A Sälker *et al* 2023 *J. Phys. D: Appl. Phys.* **56** 475301

View the article online for updates and enhancements.



This content was downloaded from IP address 134.130.185.7 on 30/08/2023 at 14:52

OPEN ACCESS
IOP Publishing
Journal of Physics D: Applied Physics
J. Phys. D: Appl. Phys. **56** (2023) 475301 (10pp)
https://doi.org/10.1088/1361-6463/ace9e3

Computer vision assisted decomposition analysis of atom probe tomography data

Janis A Sälker*, Raheleh Hadian, Jochen M Schneider and Marcus Hans

Materials Chemistry, RWTH Aachen University, Kopernikusstr. 10, D-52074 Aachen, Germany

E-mail: saelker@mch.rwth-aachen.de

Received 31 March 2023, revised 28 June 2023
Accepted for publication 24 July 2023
Published 29 August 2023

Abstract

While atom probe tomography (APT) offers 3D spatially-resolved compositional characterization at the nanometer scale, individual inspection of large datasets is time demanding and the interpretation thereof is highly operator-dependent. Recently, the decomposition behavior of (V,Al)N thin films was investigated by APT. The conventional analysis, employing standard tools from commercial software, is laborious and only a small fraction (below 5%) of the total acquired data has been used. In the present work, the analysis workflow is automated, taking into account more than 90% of the total acquired data. As a first step, the decomposition products, including matrix and enriched phases, were identified via deep learning-based semantic image segmentation. Performance of the 'matrix' and the decomposition product 'aluminum-rich' was very good, achieving F1-scores of 0.994 and 0.943, respectively, while performance for 'vanadium-rich' was with 0.854 slightly lower. The segmentation enables the investigation of phase formation evolution over temperature. As a next step, early stages of the spinodal decomposition were probed on the 'matrix' phase by a neighborhood analysis. While results were consistent with prior work, the data analysis in this work is statistically more robust by leveraging an order of magnitude larger dataset. In the end, the transferability of the presented phase segmentation workflow of the (V,Al)N-based model is shown and discussed for the decomposition of isostructural (Ti,Al)N.

Keywords: VAlN, TiAlN, deep learning, spinodal decomposition, semantic segmentation

(Some figures may appear in color only in the online journal)

1. Introduction

Recently, the decomposition behavior of $(V_{0.64}Al_{0.36})_{0.49}N_{0.51}$ thin films was investigated by a variety of methods, including x-ray diffraction, transmission electron microscopy (TEM) techniques, atom probe tomography (APT) as well as nanoindentation and resistivity measurements [1]. Sensitivity for the detection of the onset of thermal decomposition in (V,Al)N varied greatly between said characterization techniques. Diffraction and nanoindentation data indicated the wurtzite AlN formation after vacuum annealing at 900 °C, while resistivity measurements were sensitive for phase transformations already at 800 °C. The onset of thermal decomposition was identified, using TEM and APT, at 700 °C by the observation of aluminum enrichment at grain boundaries and triple

* Author to whom any correspondence should be addressed.

Original content from this work may be used under the terms of the Creative Commons Attribution 4.0 licence. Any further distribution of this work must maintain attribution to the author(s) and the title of the work, journal citation and DOI.

 © 2023 The Author(s). Published by IOP Publishing Ltd

junctions. In particular, APT data revealed compositional variations of aluminum and vanadium within the grains beyond the count rate statistics, which could be explained by spinodal decomposition.

For APT, the analysis was done either qualitatively or, in case of the compositional variations, only on small subvolumes (below 5% of the total volume). While this approach was successful, consistent analysis of larger datasets is challenging as well as time consuming. Here, automated and scalable algorithms and workflows can enable higher throughput and more reproducible results [2]. Additionally, there is room for a statistically more robust analysis, where ideally all available APT data is used.

An efficient way to address these challenges is the exploitation of machine learning (ML) methods for APT data analysis. ML applications were reported on a variety of APT data types, both raw and refined. Principal component analysis and mixture models have been used on ion time-of-flight data to investigate phase changes [3] and to determine the probability mass function [4], respectively. To automatically gather crystallographic information from appropriate systems, deep learning-based image classification has been applied to detector hit maps [5]. Aside from these approaches [3–5], which utilize the raw data directly, many ML algorithms in the literature use the reconstructed atom positions as main input [6–12]. This includes the analysis of clustering, where several approaches have been developed for APT data [6–9]. There are also studies available, for which the 3D point cloud data is transformed into 2D image representations before further investigations. Examples include phase identification of nanoscale L1(2) ordered structures [10], mapping of grain boundary composition [11] or phase segmentation by edge detection [12]. Several deep learning-based approaches for APT data produce simulated training data for supervised learning strategies [5, 10, 11], which can be beneficial as it easily provides labels, where labels are otherwise hard to obtain for dense 3D APT data. However, it is challenging for simulated data to fully capture the complexity of experimental APT data [5, 10].

In the present study we therefore evaluate the viability of supervised learning from multiple APT measurements. A comparatively large dataset describing the decomposition behavior of (V,Al)N thin films containing 13 APT measurements is used, covering the as deposited state as well as annealed material in the range of 600 °C–1100 °C. Deep learning based semantic image segmentation is applied to 2D image representations of the 3D APT data to identify three phases: Al-rich and V-rich phases as well as the remaining matrix. For Al- and V-rich phases the decomposition was investigated by a phase fraction analysis, while an atomic neighborhood analysis was applied for the matrix phase to identify the onset of spinodal decomposition.

Compared to the previous publication discussed above [1], the present work relies only on reconstructed APT data to investigate the decomposition behavior of (V,Al)N by an automated and operator bias reduced workflow. Finally, transferability of the (V,Al)N-based model is demonstrated for the decomposition of isostructural (Ti,Al)N.

2. Experimental part

2.1. Introduction to APT

APT is a three-dimensional characterization technique to explore the chemical composition of materials at nanometer scale [13]. It combines mass spectrometry and projection microscopy. A so-called DC standing voltage is applied to a thin, needle shaped specimen and either by voltage or laser pulse assisted field evaporation, surface atoms are evaporated from the specimen surface [14]. In the vicinity of the electric field, ionization takes place and eventually these ions are registered on a position-sensitive detector. The time between the application of the pulse and the detection of the ion, known as the time-of-flight, allows for the calculation of a mass-to-charge ratio, which is used to identify the elemental nature of the ion [14]. A crucial step in APT analysis is the reconstruction process of the original specimen, where the 2D detector positions are projected back to the approximate original 3D positions. The effective spatial resolution limit of APT is $\sim$1 nm [15, 16].

2.2. APT data

For this work, previously published APT data of (V,Al)N [1, 17] and (Ti,Al)N [18] are used. Primary analysis is done on (V,Al)N, while (Ti,Al)N data is used as a demonstrator for the transferability of the learned model to a chemically and structurally similar material system. All APT specimens were obtained from thin films prepared by high power pulsed magnetron sputtering employing a $V_{0.6}Al_{0.4}$ or a $Ti_{0.5}Al_{0.5}$ target in reactive Ar/N_2 atmosphere. Deposition temperatures were 440 °C and 300 °C for (V,Al)N and (Ti,Al)N, respectively. Substrate material was either sapphire (0001) or NaCl. For the latter case, the NaCl was solved in distilled water and the dissolved material has been ground to produce thin film flakes. Four specimens were prepared from as deposited samples, while the remaining samples were annealed in high vacuum (thin films) or argon atmosphere (thin film flakes) between temperatures of 600 °C and 1200 °C for 30 minutes. An overview of the entire dataset is given in table 1.

Atom probe specimens were prepared from thin films in cross-section and plan-view lift-out geometries (see supplementary information of Hans *et al* [1]) as well as from thin film flakes. APT analysis was carried out using a CAMECA LEAP 4000X HR and employing laser pulse assisted field evaporation. Reconstruction was done based on shank angles and voltage evolution for (V,Al)N and (Ti,Al)N specimens, respectively. Additional information regarding deposition, annealing and APT parameters for the (V,Al)N thin films [1] and thin film flakes [17] as well as the (Ti,Al)N thin films [18] samples are available in the respective publications.

Table 1. Material system, APT specimen lift-out, annealing temperature, atomic density and chemical composition of the APT samples [19]. Remaining compositional contributions are attributed to O, C, Ga and Ar impurities which are in sum <2 at.%.

Material system	Lift-out from	Annealing temperature (°C)	Atomic density (atoms nm^{-3})	Chemical composition (at.%)			
				V	Ti	Al	N
(V,Al)N	Film flake	As deposited	18.5	31.9	–	18.3	47.9
		900	18.3	29.0	–	21.1	48.2
		1100	18.4	28.8	–	23.6	46.6
	Film plan-view	As deposited	19.4	33.4	–	19.8	45.9
		600	20.0	33.7	–	21.3	44.6
		700	19.1	32.9	–	19.0	47.5
		800	18.9	32.3	–	21.3	45.5
	Film cross-section	As deposited	18.6	33.7	–	18.2	47.4
		600	18.6	33.9	–	18.2	47.2
		700	18.5	32.1	–	19.9	47.3
		800	18.3	26.6	–	25.4	47.1
		900	18.3	23.7	–	29.0	46.2
		1000	20.3	29.4	–	28.4	41.2
(Ti,Al)N		As deposited	18.0	–	27.2	26.4	45.8
		850	17.9	–	23.4	30.5	45.6
		1200	18.1	–	25.4	30.4	43.5

3. Computational part

3.1. Data preparation

To convert the reconstructed 3D atomic positions to images, data must first be transformed to voxels using a fixed 3D grid (figure 1(a)). In each voxel, the vanadium and aluminum content was obtained. Nitrogen was omitted since it does not add further information relevant for the decomposition. The selection of the voxel size is dataset specific and depends on the individual consideration between the resolution (improved by smaller voxel size) and the statistical error of the composition measurement (improved by larger voxel size). For this work, the average atomic density of a sample ranges between 17.9 and 20.3 atoms nm^{-3} (see table 1). Due to the small differences in density between samples, which indicates similar reconstruction quality, a common voxel size of $1 \times 1 \times 1$ nm^3 was chosen.

For each voxel, as a first step, the vanadium and aluminum content is obtained. Images are created along the x- and y-axis of the 3D grid. Each voxel corresponds to one pixel of an x-axis image and one pixel of a y-axis image. An image consists of two channels, which display the vanadium and aluminum concentrations as grayscale values (figure 1(b)). Voxels that do not contain any vanadium or aluminum atoms therefore correspond to black pixels and can be classified as background. Due to the shape and size variations of APT samples, the content of background pixels may vary strongly. A constant image size of 608×192 pixel was sufficient to capture all APT reconstructions without resizing.

The segmentation model is trained to identify four classes: Background, matrix as well as V-rich and Al-rich phases (figure 1(c)). Labels for all classes were created by a combination of image processing techniques and manual refinement. Each training example consists of the two-channel input image and the respective label/mask. Both input channels are necessary to properly distinguish the empty background from V- and Al-depleted phase areas near the sample border, as seen at the top part of the aluminum input in figure 1(b) (emphasized with an arrow).

3.2. Training procedure

Training data was prepared from nine (V,Al)N APT samples, consisting of x- and y-axis image stacks from sample groups 'film flake' (from as deposited to 1100 °C) and 'film cross-section' (from as deposited to 1000 °C). It contains data from specimens in the as deposited state up to the annealing temperature of 1100 °C and therefore incorporates information from all present stages of the decomposition of (V,Al)N. A total of 1822 training images were prepared, of which 20% were used for validation. Additionally, the training set was augmented by randomly flipping images horizontally or vertically during training. For the segmentation model, a U-Net [20] structure was selected, which was originally developed for biomedical images. An architecture with layer dimensions of 32, 64, 128 and 256 was employed. The model was trained for 150 epochs [21] with a batch size of 20 and a combination of dice and cross-entropy loss [22]. The initial learning rate was set to 0.001 and was reduced every 30 epochs by 0.8. A single NVIDIA Volta 100 GPU (16 GB) was used for training.

After inference, the segmented images were transformed back to atoms by correlating the pixels to the original voxel positions and retrieving the atoms from those voxels. Each atom in a voxel will be assigned to the same predicted class. In principle, either the x- or y-axis data is sufficient, however, the combination of multiple viewing axes may help recover some of the information loss caused by the transformation from 3D to 2D. If there is a disagreement between two predictions of

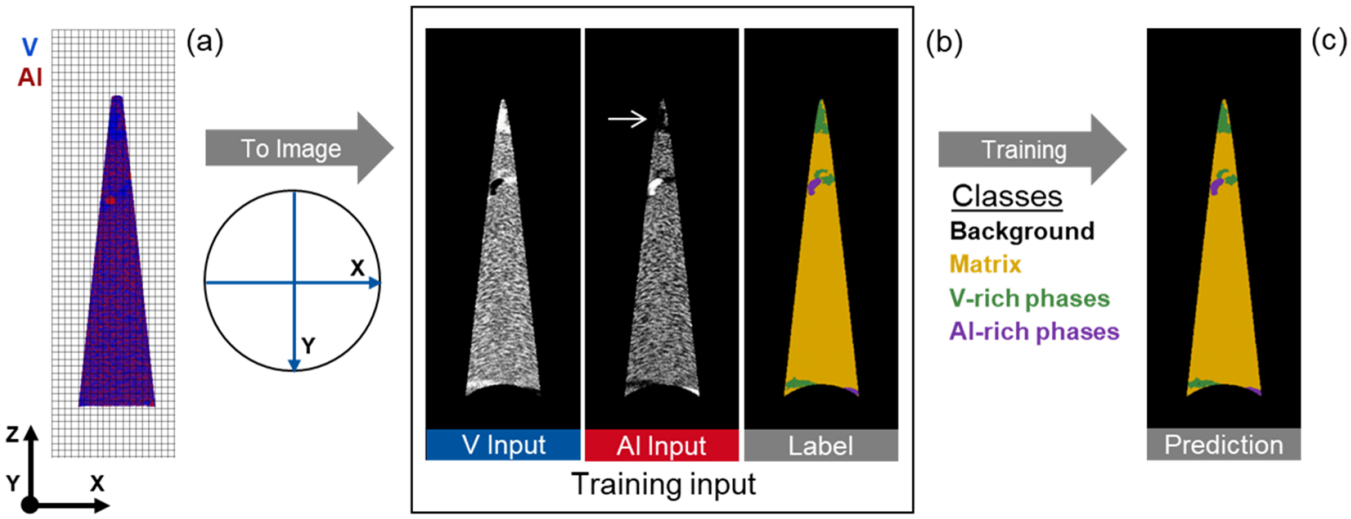


Figure 1. Voxelization of the 3D reconstructed APT data using a grid of $1 \times 1 \times 1$ nm^3 sub volumes (a). In each voxel, the vanadium and aluminum concentration is calculated. These values are converted into grayscale for images created along the *x*- and *y*-axis of the 3D grid. Training images consist of two-channels (vanadium and aluminum inputs). The arrow in the Al-input image marks an Al-depleted phase, with no clear border to the background class (b). Together with the prior created labels, the model is trained to identify four classes: Background, matrix, V-rich phase, and Al-rich phase (c). The example shows a lift-out from (V,Al)N film flake after annealing at 1100 °C.

a voxel, the class probabilities of the last network layer were averaged and used to determine the final assignment.

Performance evaluation of the deep learning model was done on the image level. For each pixel and class, the prediction and label either match (true positive (TP) or true negative (TN)) or mismatch (false positive (FP) or false negative (FN)). The metrics used for evaluation are intersection over union (IoU), F1-score, precision and recall, which are defined as:

$$\text{IoU} = \frac{\text{TP}}{\text{TP} + \text{FP} + \text{FN}} \tag{3.1}$$

$$\text{Precision} = \frac{\text{TP}}{\text{TP} + \text{FP}} \tag{3.2}$$

$$\text{Recall} = \frac{\text{TP}}{\text{TP} + \text{FN}} \tag{3.3}$$

$$\text{F1-score} = 2 \times \frac{\text{Precision} \times \text{Recall}}{\text{Precision} + \text{Recall}} \tag{3.4}$$

IoU is the most widely used metric for segmentation and object detection [23], while precision and recall can give more insight into specific aspects of the prediction. Precision is the fraction of relevant classes among the retrieved classes, while recall is the fraction of relevant classes that were retrieved. F1-score is the harmonic mean of both precision and recall.

3.3. Neighborhood ratio

To evaluate the onset of spinodal decomposition, the atomic environment of the identified matrix phase was investigated using a simple neighborhood analysis. Approaches based on nearest neighborhoods have been commonly used for APT data [14]. Aluminum was chosen as the query element because of its stronger tendency for segregation (aluminum has a 25% lower activation energy for bulk diffusion compared to vanadium [1]). It is also present in both discussed material systems, (V,Al)N and (Ti,Al)N.

For each aluminum atom of a sample, the 400 nearest atomic neighbors were considered. Occurrences of each species were summed over all query aluminum atoms to formulate a single ratio *Al neighbors/total neighbors*. To compensate for differences in composition, the ratio was normalized by the aluminum content of the respective sample. Values greater than 1 therefore indicate local aluminum agglomerations beyond what would be expected based on the average composition. The influence of the neighborhood size on the results was minimal above 300 neighbors. While other methods can provide more descriptive characteristics, such as the wavelength or amplitude of the spinodal decomposition [24], we used the normalized neighborhood ratio specifically for its simplicity.

4. Results and discussion

4.1. Phase identification

The model performance per class/phase is shown in table 2.

Classes background and matrix achieve ideal or near ideal metrics. These are often trivial to distinguish, especially at lower annealing temperatures, and are responsible for 99.4% (87.6% background + 11.8% matrix) of the overall pixel count. A representative example is given in figure 2(a).

For V- and Al-rich phases, F1-scores of 0.854 and 0.943 were achieved, respectively. Misclassification occurred almost exclusively between the matrix and the respective enriched phases. The discrepancy in performance of V- and Al-rich phases could be attributed to differences in composition and decomposition behavior. In the matrix phase, the vanadium

Table 2. Performance on the image validation set.

	Background	Matrix	V-rich	Al-rich	Mean
IoU	0.999	0.989	0.745	0.891	0.906
F1	0.999	0.994	0.854	0.943	0.948
Precision	0.999	0.994	0.853	0.950	0.949
Recall	0.999	0.994	0.855	0.935	0.946

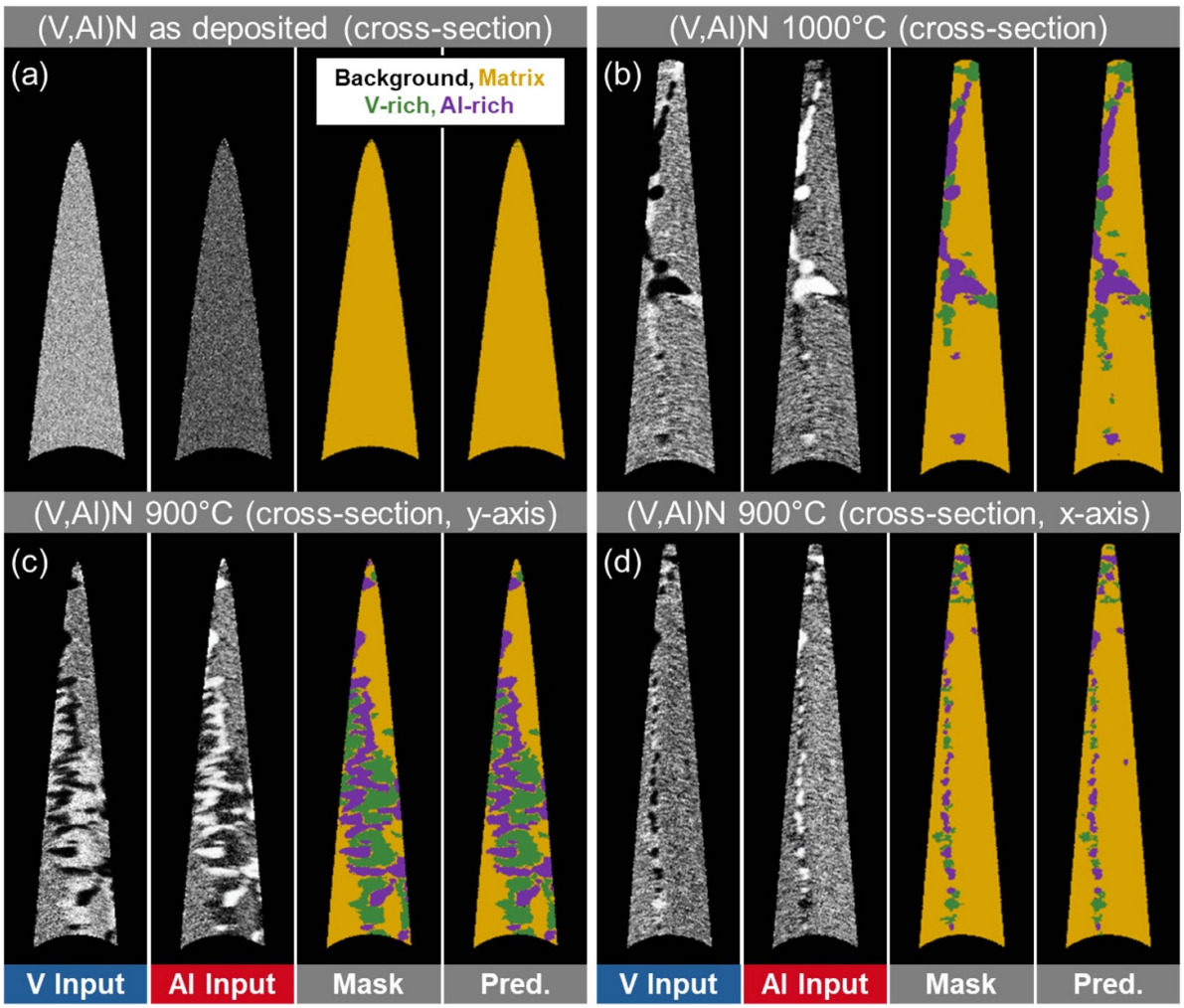


Figure 2. Input images, masks and predictions of the validation set for samples of (V,Al)N film cross-section as deposited (a), 1000 °C (b), 900 °C (*y*-axis) (c) and 900 °C (*x*-axis) (d). Each set of images corresponds to data from a single 2D slice near the sample center. Black background of images was cut for visualization purposes.

content is on average 9 at.% higher than the aluminum content. In addition, the enrichment of V-rich phases is not as strong as that of Al-rich phases, which will be further discussed in section 4.2. The smaller compositional difference of V-rich phases towards the matrix leads to a lower contrast in the input images, which makes identification more challenging. An example is given in figure 2(b), which emphasizes a higher uncertainty towards the V-rich phases. This problem gets more severe at higher annealing temperatures, where thermal decomposition by spinodal decomposition and nucleation and growth gets increasingly more difficult to distinguish. In cases where both V- and Al-rich phases are equally pronounced, predictions are often similar in quality, as shown in figure 2(c).

Since two sets of images (*x*- and *y*-axis) were prepared per sample and subsequently predicted, there are two segmentations per sample available. These may offer very different views on the sample, as seen when comparing figures 2(c) and (d) which display the same sample from the *y*- and *x*-axis perspective, respectively. The percentage of disagreement between both predictions positively correlates with the content of V-rich phases (displayed in figure 4), which indicates again the difficulty of the model to identify this class. When considering only non-empty voxels (excluding the background) the

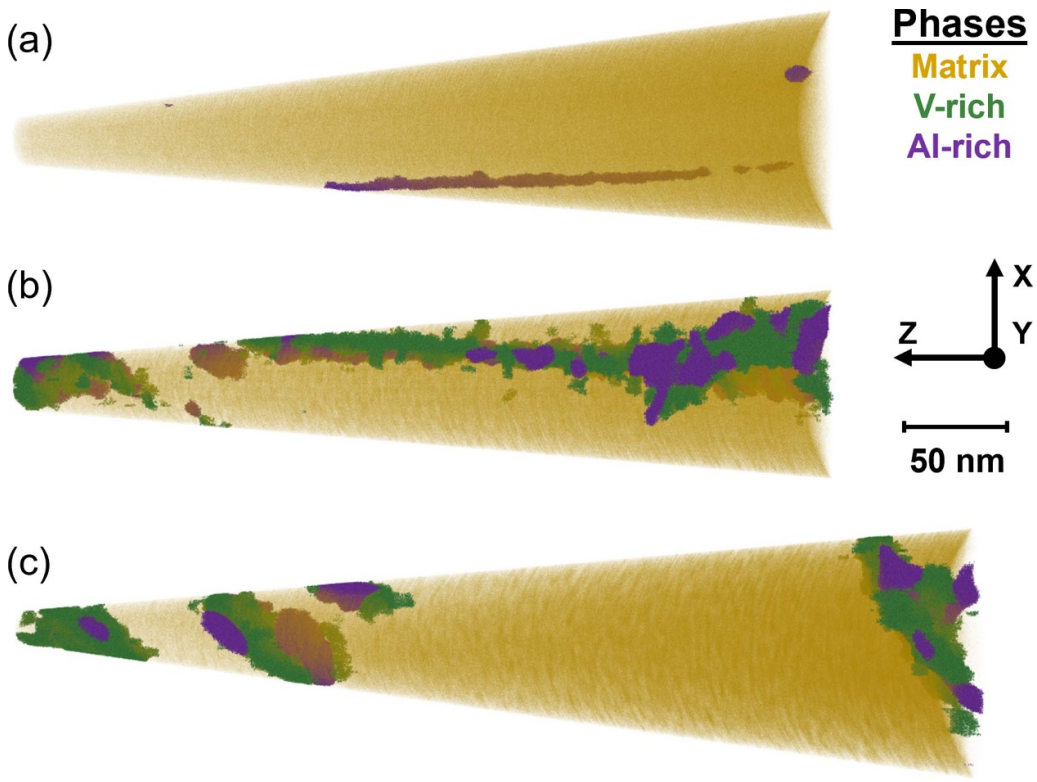


Figure 3. Segmented APT point data of (V,Al)N cross-section 700 °C (a) and 900 °C (b), and (V,Al)N film flake 1100 °C (c). Atoms are colored based on the results of the phase segmentation model. Due to differences in measurement yield, reconstructions vary in size.

maximum disagreement in predictions between the two axes was 4.5% for (V,Al)N film cross-section at 1000 °C.

4.2. Phase analysis

When combining all predicted images as described in section 3.2, segmented APT point data can be restored. Figure 3 shows three APT samples which were colored based on the results of the phase segmentation model. It is visible, that V- and Al-rich phases often form closely together. In addition, grain boundaries are visible in figures 3(a) and (b), which were identified in previous work, among triple junctions, to be the starting location for decomposition based on nucleation and growth [1]. Hence, the linear Al-rich feature is most likely a triple junction of the columnar grain boundaries [1], i.e. the volume located in growth direction in between three adjacent columnar grains.

Quantitative results of V- and Al-rich phase contents as well as their enrichment are presented in figure 4. The first Al-rich phases were identified at 700 °C, while the presence of V-rich phases was detected at 800 °C (figure 4 top). Generally, phase contents increase with rising annealing temperature, reaching its maximum for the cross-section sample at 1000 °C with 9.7% and 9.3% for V-rich and Al-rich phases, respectively. Due to the high locality of APT, phase contents may strongly depend on the specific lift-out location, which makes their comparison in terms of decomposition evolution difficult. A good example is that of the two 700 °C samples, where a large grain boundary was captured in the cross-section sample (visible in figure 3(a)), while for the plan-view sample only traces of a triple junction were identified.

An alternative criterion is the increasing enrichment of the V- and Al-rich phases (figure 4 bottom). Over the entire dataset, an increase from 37 to 47 at.% and 40 to 55 at.% is visible for vanadium and aluminum, respectively. Previous work on these data confirmed the formation of Al-rich grain boundaries and triple junctions at 700 °C [1]. The delayed formation and lower enrichment of V-rich phases can be explained by the difference in bulk diffusion barriers. For an aluminum content of 25 at.%, the activation energy for bulk diffusion of aluminum is 25% lower compared to vanadium, enabling a higher mobility of aluminum [1].

Besides the nucleation and growth of secondary phases, spinodal decomposition is investigated in the matrix phase, where greater analysis volume and statistics can be leveraged. The prior performed phase segmentation is a crucial prerequisite for this analysis, as the compositional changes during the onset of spinodal decomposition are not as pronounced as for the nucleation of growth of secondary phases [25]. Larger contents of V- and Al-rich phases would therefore influence the neighborhood ratio disproportionately and no separate evaluation of the spinodal decomposition would be possible. Results of the neighborhood ratio of aluminum atoms are shown in figure 5.

Neighborhood ratios of samples up to a temperature of 600 °C have constant values close to 1, meaning that the local neighborhood of aluminum atoms is very similar to the samples overall chemical composition. At 700 °C, there is a small increase for both cross-section and plan-view

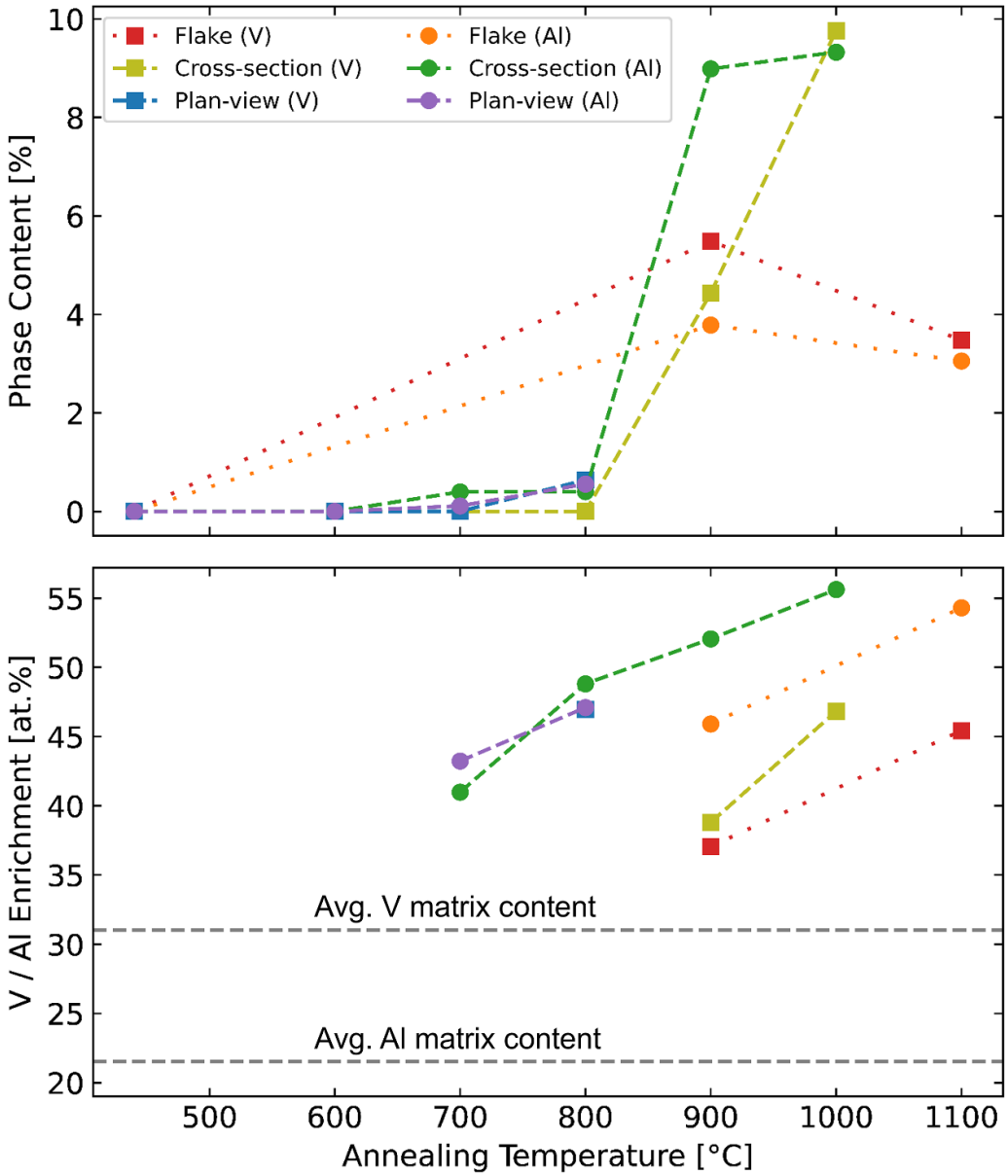


Figure 4. Phase content (top) and enrichment (bottom) of identified V-rich and Al-rich phases. The average vanadium and aluminum matrix content is in relation to the entire dataset. Connecting lines for film flake samples only serve as visual guidance.

samples visible. This is an indication for the onset of the spinodal decomposition, showing that aluminum is enriched locally. Values for all samples increase with higher annealing temperatures, indicating the progress of spinodal decomposition. Differences between sample groups at similar temperatures may be attributed to the different APT lift-out locations and the small volume probed by APT.

Hence, based on the phase and neighborhood analysis of the reconstructed APT data presented above, an automated workflow, reducing operator bias, has been designed. As a next step, we evaluate the transferability of this workflow to the material system (Ti,Al)N as its thermal decomposition is also characterized by spinodal decomposition [18].

4.3. Transfer of the model to (Ti,Al)N

Contrary to (V,Al)N, where spinodal decomposition proceeds simultaneously with nucleation and growth [1], the decomposition in (Ti,Al)N progresses sequentially. For $(Ti_{0.34},Al_{0.66})N$, decomposition is purely spinodal until ∼900 °C after which nucleation and growth of wurzite AlN begins [26, 27]. Three $(Ti_{0.51},Al_{0.49})_{0.47}N_{0.53}$ APT specimens were investigated, one as deposited (film growth at 300 °C) and two vacuum annealed at 850 °C and 1200 °C (table 1). The used thin films were overstoichiometric with respect to nitrogen, which is common for films produced in industrial deposition systems [18]. This is not reflected in the APT measured composition shown in

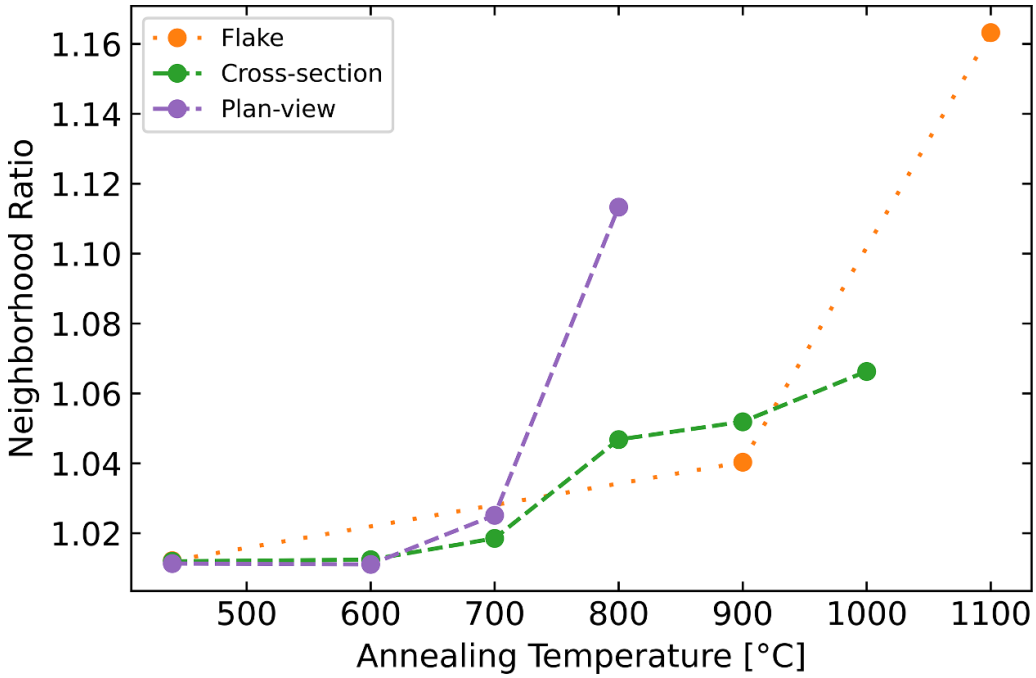


Figure 5. Normalized neighborhood ratio according to section 3.3, calculated for aluminum atoms with a neighborhood size of 400. Connecting lines for film flake samples only serve as visual guidance.

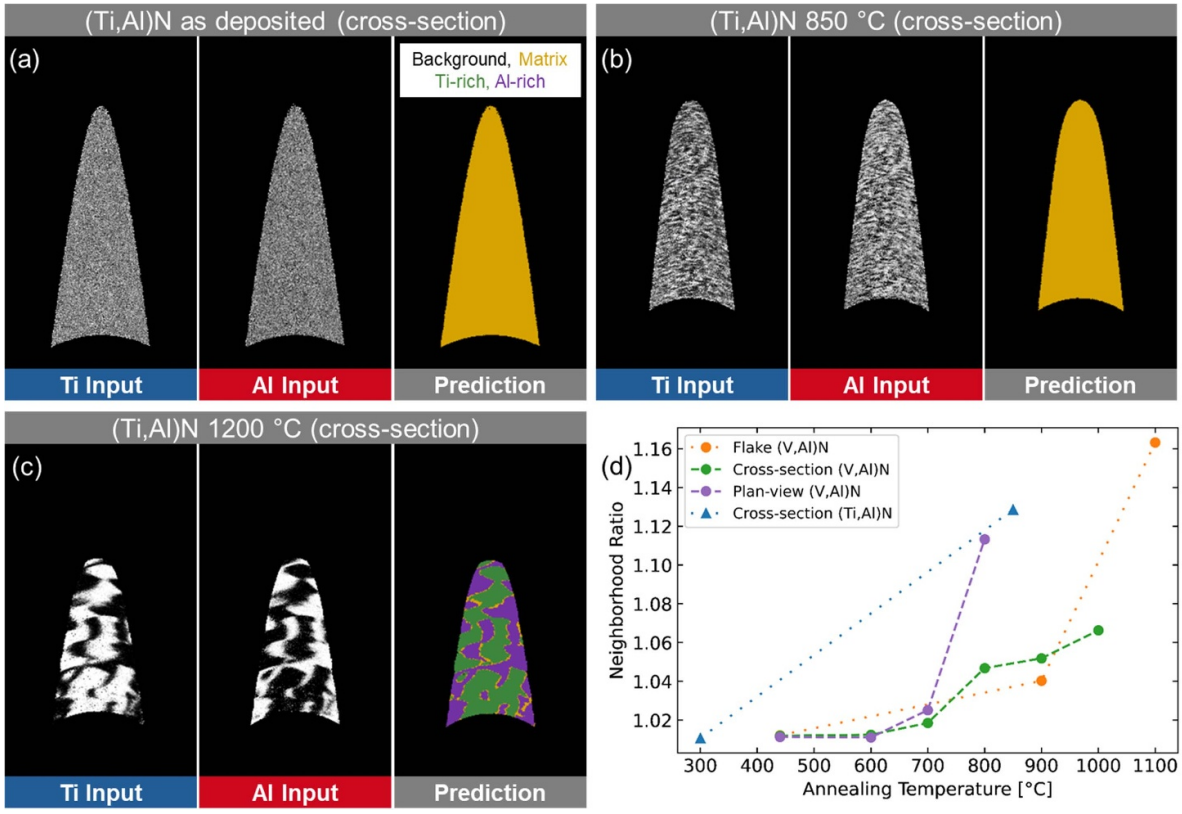


Figure 6. Input images and predictions for samples of (Ti,Al)N film cross-section as deposited (a), 850 °C (b) and 1200 °C (c). Normalized neighborhood ratio of aluminum atoms for previously shown (V,Al)N and added (Ti,Al)N samples (d). Connecting lines for (V,Al)N film flake and (Ti,Al)N samples only serve as visual guidance.

table 1, due to the underestimation of nitrogen content, caused by the electric field strength-dependent accuracy of (Ti,Al)N composition measurements by APT [28].

First, the phase segmentation model was tested, where contributions of vanadium were exchanged with titanium. No additional training or changes were conducted to the model. Typical input pairs and their prediction are shown for each (Ti,Al)N sample in figures 6(a)–(c).

For the as deposited and 850 °C annealed sample, 100% and 99.8% of the atoms were predicted as the matrix phase, respectively. This result is in agreement with prior work, where no presence of enriched wurtzite AlN was found until 850 °C by x-ray diffraction [18]. At 1200 °C, the sample is fully decomposed into Ti- and Al-rich phases, for which there was no similar stage of decomposition in the (V,Al)N training data. Most atoms were correctly identified to be part of Ti- or Al-rich phases, while around 7.4% of the atoms were misclassified as the matrix phase, predominantly at phase borders. While these regions showed indeed less enrichment, they share no further similarity with the actual matrix phase of the training APT data.

The decomposition of the matrix can also be estimated via the discussed neighborhood ratio, which is displayed in figure 6(d). The ratio of the as deposited (Ti,Al)N sample (300 °C) is in good agreement with the as deposited and 600 °C annealed (V,Al)N samples. At 850 °C, the neighborhood ratio indicates strong spinodal decomposition, which is also visible by the local enrichments of titanium and aluminum in figure 6(b). The absolute value is comparable to the (V,Al)N 800 °C plan-view sample. Generally, a stronger tendency for decomposition is expected for (Ti,Al)N at similar aluminum contents, due to the higher driving force for decomposition of (Ti,Al)N, which is reflected by the mixing enthalpy [17, 29]. The 1200 °C sample was omitted, since its initial matrix is fully decomposed and therefore no comparable analysis was possible.

Therefore, spinodal decomposition of (Ti,Al)N could be identified by the automated workflow, that was designed for the (V,Al)N system and reduces operator bias.

5. Conclusions

We have investigated the thermal decomposition of (V,Al)N thin films using computer vision assisted analysis of APT data. Experimental data was used to train an image-based semantic segmentation model to identify phases formed during thermal decomposition, induced by annealing. Performance of the 'matrix' and the decomposition product 'aluminum-rich' was very good, achieving F1-scores of 0.994 and 0.943, respectively, while performance for 'vanadium-rich' was with 0.854 slightly lower. This is likely due to the less pronounced decomposition of vanadium, caused by higher activation energies of bulk diffusion and overall smaller compositional differences towards the matrix phase. Early stages of the spinodal decomposition were probed on the separated matrix phase by a neighborhood analysis. While results were consistent with prior work, the current data analysis is statistically more robust by leveraging an order of magnitude larger dataset. The transferability of the presented phase segmentation workflow of the (V,Al)N based model was shown and discussed for the thermal decomposition of isostructural (Ti,Al)N. The present data-driven approach allowed for an automated analysis to investigate a series of reconstructed APT samples in a consistent manner, significantly reducing the operator bias inherent in manual evaluations of multiple measurements.

Data availability statement

The data that support the findings of this study are openly available at the following URL/DOI: https://doi.org/10.5281/zenodo.7788883.

Acknowledgments

The authors gratefully acknowledge the German Federal Ministry of Education and Research (BMBF) and the Ministry for Culture and Science of the State of North Rhine-Westphalia (MKW NRW) for supporting this work as part of the NHR funding. The authors gratefully acknowledge the computing time provided to them on the high performance computer CLAIX at the NHR Center NHR4CES. This is funded by the German Federal Ministry of Education and Research and the Ministry for Culture and Science of the State of North Rhine-Westphalia. The computations for this research were performed using computing resources under project rwth1223. Moreover, the authors acknowledge financial support from the German Research Foundation (DFG) within the Project 515702322 (HA 9139/1-1, SCHN 735/50-1).

ORCID iDs

Janis A Sälker https://orcid.org/0009-0007-1495-2781
Raheleh Hadian https://orcid.org/0000-0002-9616-4602
Jochen M Schneider https://orcid.org/0000-0003-1239-1961
Marcus Hans https://orcid.org/0000-0002-1814-3101

References

[1] Hans M, Czigány Z, Neuß D, Sälker J A, Rueß H, Krause J, Nayak G K, Holec D and Schneider J M 2022 Probing the onset of wurtzite phase formation in (V,Al)N thin films by transmission electron microscopy and atom probe tomography *Surf. Coat. Technol.* **442** 128235

[2] Kühbach M, Bajaj P, Zhao H, Çelik M H, Jägle E A and Gault B 2021 On strong-scaling and open-source tools for analyzing atom probe tomography data *npj Comput. Mater.* **7** 21

[3] Sarker J, Broderick S, Bhuiyan A F M A U, Feng Z, Zhao H and Mazumder B 2020 A combined approach of atom probe tomography and unsupervised machine learning to understand phase transformation in $(Al_xGa_{1-x})_{(2)}O_3$ *Appl. Phys. Lett.* **116** 5

[4] Coakley K J and Sanford N A 2022 Learning atom probe tomography time-of-flight peaks for mass-to-charge ratio spectrometry *Ultramicroscopy* **237** 9
[5] Wei Y, Gault B, Varanasi R S, Raabe D, Herbig M and Breen A J 2018 Machine-learning-based atom probe crystallographic analysis *Ultramicroscopy* **194** 15–24
[6] Wang J, Schreiber D K, Bailey N, Hosemann P and Toloczko M B 2019 The application of the OPTICS algorithm to cluster analysis in atom probe tomography data *Microsc. Microanal.* **25** 338–48
[7] Zelenty J, Dahl A, Hyde J, Smith G D W and Moody M P 2017 Detecting clusters in atom probe data with Gaussian mixture models *Microsc. Microanal.* **23** 269–78
[8] Ghamarian I and Marquis E A 2019 Hierarchical density-based cluster analysis framework for atom probe tomography data *Ultramicroscopy* **200** 28–38
[9] Vincent G B, Proudian A P and Zimmerman J D 2021 Three dimensional cluster analysis for atom probe tomography using Ripley's K-function and machine learning *Ultramicroscopy* **220** 7
[10] Li Y, Zhou X, Colnaghi T, Wei Y, Marek A, Li H, Bauer S, Rampp M and Stephenson L T 2021 Convolutional neural network-assisted recognition of nanoscale L1(2) ordered structures in face-centred cubic alloys *npj Comput. Mater.* **7** 9
[11] Zhou X Y, Wei Y, Kühbach M, Zhao H, Vogel F, Darvishi Kamachali R, Thompson G B, Raabe D and Gault B 2022 Revealing in-plane grain boundary composition features through machine learning from atom probe tomography data *Acta Mater.* **226** 15
[12] Madireddy S, Chung D-W, Loeffler T, Sankaranarayanan S K R S, Seidman D N, Balaprakash P and Heinonen O 2019 Phase segmentation in atom-probe tomography using deep learning-based edge detection *Sci. Rep.* **9** 10
[13] Blavette D, Bostel A, Sarrau J M, Deconihout B and Menand A 1993 An atom probe for three-dimensional tomography *Nature* **363** 432–5
[14] Gault B, Moody M P, Cairney J M and Ringer S P 2012 *Atom Probe Microscopy* (*Springer Series in Materials Science* vol 160) (Springer) (https://doi.org/10.1007/978-1-4614-3436-8)
[15] De Geuser F and Gault B 2020 Metrology of small particles and solute clusters by atom probe tomography *Acta Mater.* **188** 406–15
[16] Gault B *et al* 2021 Reflections on the spatial performance of atom probe tomography in the analysis of atomic neighborhoods *Microsc. Microanal.* **28** 1116–26
[17] Hans M, Rueß H, Czigány Z, Krause J, Ondračka P, Music D, Evertz S, Holzapfel D M, Primetzhofer D and Schneider J M 2020 Spinodal decomposition of reactively sputtered (V0.64Al0.36)0.49N0.51 VAlN thin films *Surf. Coat. Technol.* **389** 125641
[18] Baben M T, Hans M, Primetzhofer D, Evertz S, Ruess H and Schneider J M 2017 Unprecedented thermal stability of inherently metastable titanium aluminum nitride by point defect engineering *Mater. Res. Lett.* **5** 158–69
[19] Sälker J A and Hans M 2023 Dataset for Computer vision assisted decomposition analysis of atom probe tomography data *Zenodo* (https://doi.org/10.5281/zenodo.7788883)
[20] Ronneberger O, Fischer P and Brox T 2015 *U-Net: Convolutional Networks for Biomedical Image Segmentation* (*Medical Image Computing and Computer-Assisted Intervention – MICCAI*) (Springer) pp 234–41
[21] Goodfellow I, Bengio Y and Courville A 2016 *Deep Learning* (MIT Press)
[22] Jadon S J 2020 A survey of loss functions for semantic segmentation (arXiv:2006.14822)
[23] Rezatofighi H *et al* 2019 Generalized intersection over union: a metric and a loss for bounding box regression pp 658–66 (arXiv:1902.09630)
[24] Guo W, Garfinkel D A, Tucker J D, Haley D, Young G A and Poplawsky J D 2016 An atom probe perspective on phase separation and precipitation in duplex stainless steels *Nanotechnology* **27** 254004
[25] Cahn J W 1961 On spinodal decomposition *Acta Metall.* **9** 795–801
[26] Mayrhofer P H, Hörling A, Karlsson L, Sjölén J, Larsson T, Mitterer C and Hultman L 2003 Self-organized nanostructures in the Ti-Al-N system *Appl. Phys. Lett.* **83** 2049–51
[27] Hörling A, Hultman L, Odén M, Sjölén J and Karlsson L 2002 Thermal stability of arc evaporated high aluminum-content $Ti_{1-x}Al_x$ N thin films *J. Vac. Sci. Technol.* A **20** 1815–23
[28] Hans M and Schneider J M 2020 Electric field strength-dependent accuracy of TiAlN thin film composition measurements by laser-assisted atom probe tomography *New J. Phys.* **22** 9
[29] Holec D, Rachbauer R, Chen L, Wang L, Luef D and Mayrhofer P H 2011 Phase stability and alloy-related trends in Ti-Al-N, Zr-Al-N and Hf-Al-N systems from first principles *Surf. Coat. Technol.* **206** 1698–704